Quasi-elastic scattering and spin-phonon coupling in Se-substituted $NiPS_3$

Deepu Kumar,[1] Rajesh Kumar Ulaganathan,[2] Raju Kalaivanan,[3] Raman Sankar,[2,*] Maeng-Je Seong,[1,†] and Kwang-Yong Choi[4,‡]

[1]*Department of Physics and Center for Berry Curvature-based New Phenomena (BeCaP), Chung-Ang University, Seoul 06974, Republic of Korea*

[2]*Institute of Physics, Academia Sinica, Nankang, Taipei 11529, Taiwan*

[3]*Centre for Nanotechnology, Indian Institute of Technology Roorkee, 247667, India*

[4]*Department of Physics, Sungkyunkwan University, Suwon 16419, Republic of Korea*

(Received 11 May 2025; accepted 24 October 2025; published 18 November 2025)

Quasi-elastic scattering (QES) serves as a sensitive probe of slow spin fluctuations in low-dimensional magnetic systems, multiferroics, and frustrated quantum magnets. Here, we investigate spin and lattice dynamics in anion-substituted $NiPS_{3-x}Se_x$ using temperature- and polarization-dependent Raman spectroscopy. Above the Néel temperature, the Raman spectra in the cocircular polarization configuration show a QES response near zero frequency, which is described by a Lorentzian profile. This QES is linked to paramagnetic spin fluctuations and the associated energy density of spins, which are slightly suppressed with increasing Se content. Notably, even inside the magnetically ordered state (below 50 K), we observe a strong enhancement of this QES signal, indicative of persistent fluctuations of the ordered magnetic moments. Concurrently, spin-phonon coupling manifests as an anomalous renormalization of phonon self-energy in certain phonon modes that couple strongly to the magnetic ions, with their frequencies shifting systematically as Se concentration increases. These results suggest that spin fluctuations and lattice vibrations remain strongly intertwined in $NiPS_{3-x}Se_x$, and that chemical substitution provides a means to tune this spin-phonon coupling in van der Waals magnets.

DOI: 10.1103/r2t5-vyvd

I. INTRODUCTION

Two-dimensional (2D) van der Waals magnets provide prominent platforms for exploring quantum phenomena and implementing novel spintronic functionality. In particular, transition-metal thiophosphates MPX_3 (M = Ni, Fe, Mn; X = S, Se) exhibit exceptional magnetic and topological properties, hosting diverse spin models including Heisenberg, Ising, and XXZ Hamiltonians with Néel or zigzag order [1–4].

$NiPS_3$ is an XXZ-type antiferromagnet that exhibits a zigzag magnetic structure below $T_N \sim$ 155 K whereas $MnPS_3$ ($MnPSe_3$) behaves as a Heisenberg (XY-type) antiferromagnet with Néel-type magnetic order below $T_N \sim$ 78 K (74 K) [1–3]. In contrast, $FePS_3$ is characterized as an Ising antiferromagnet with a zigzag magnetic structure below $T_N \sim$ 120 K [4]. These distinct magnetic ground states underscore the strong sensitivity of the MPX_3 family to the choice of transition-metal ion. In this context, both heterogeneous cation substitution $MM'PX_3$, where M and M' are different transition metals, and anion substitution $MP(XX')_3$, where X and X' represent different chalcogens, have been shown to tune their magnetic, excitonic, and vibrational properties in mixed compounds. For instance, even low levels of cation substitution in $Ni_{1-x}Cd_xPS_3$ [5] and $Ni_{1-x}Mn_xPS_3$ [6], as well as anion substitution in $NiPS_{3-x}Se_x$ [7], result in a significant quenching of photoluminescence emission. Furthermore, such substitutions lead to the emergence of additional phonon modes while simultaneously suppressing two-magnon excitations in the mixed systems [8–10].

Singularly, variations in nonmagnetic atoms within magnetic lattices bring about several critical phenomena, resulting from the interplay between competing magnetic interactions among magnetic atoms, varying spin-orbit coupling strengths between magnetic and chalcogen atoms, and differing degrees of magnetic anisotropy [1,3,11]. The ensuing phenomena can be effectively probed via quasi-elastic scattering (QES), which arises from slow, low-energy fluctuations of spins or energy density. Unlike coherent excitations such as magnons or phonons, which involve finite energy transfer, QES occurs with negligible energy shift, allowing it to probe dynamic fluctuations rather than purely static magnetic order. Various experimental techniques, such as neutron, x-ray, and Raman scattering, can be employed to investigate QES. Among these, Raman spectroscopy, particularly when combined with external tuning perturbations such as temperature and pressure, has proven to be a reliable, nondestructive choice of experiment [12–14]. Notably, recent studies have demonstrated that the QES response in MPX_3 compounds is highly sensitive to the specific transition-metal ion (M), highlighting the role of magnetic anisotropy and exchange interactions in governing low-energy spin dynamics [15,16].

To gain a deeper understanding of the anion substitution effect on slow, low-energy spin dynamics, we conducted in-depth temperature- and polarization-dependent Raman investigations of $NiPS_{3-x}Se_x$ (x = 0.03, 0.06, and 0.09). As expected, we observe a QES above T_N, exhibiting Lorentzian line shapes characteristic of spin energy density fluctuations.

*Contact author: sankarndf@gmail.com
†Contact author: mseong@cau.ac.kr
‡Contact author: choisky99@skku.edu

Notably, this QES persists into the magnetically ordered state, displaying anomalous behavior: the spectral profile deviates from a simple Lorentzian, and the quasi-elastic spectral weight increases significantly, reflecting enhanced fluctuations of the ordered magnetic moments. The quasi-elastic response weakens with increasing Se substitution from $x = 0.03$–0.09, while phonon modes associated with magnetic Ni^{2+} ions exhibit anomalous softening or hardening below T_N. This correlated spin and lattice dynamics demonstrate tunable spin-lattice coupling through anion substitution in $NiPS_{3-x}Se_x$.

II. RESULTS AND DISCUSSION

A. Raman scattering of $NiPS_{3-x}Se_x$

Details on sample growth and temperature-dependent unpolarized and linearly polarized Raman measurements can be found in our previous work [7]. For circularly polarized Raman measurements, we installed two quarter-wave plates, one in the incident light beam path and the other in the scattered light beam path to generate either right-(σ_R) or left- circularly (σ_L) polarized light. A linear polarizer was placed in front of the spectrometer to ensure a consistent Raman signal with respect to the grating orientation.

Bulk $NiPS_3$ possesses a monoclinic structure with the point group C_{2h}, and contains ten atoms per unit cell, resulting in 30 phonon excitations at the Γ point of the Brillouin zone classified according to the irreducible representation: $\Gamma = 8A_g + 7B_g + 6A_u + 9B_u$ [17,18]. In the linear parallel polarization (XX) configuration, both A_g and B_g modes are Raman active, while only B_g modes are allowed in the cross linear polarization (XY) configuration. Within the semiclassical approximation, the Raman scattering intensity of first-order phonon modes is expressed as $I_{\text{int}} = |\hat{e}_s^t.R.\hat{e}_i|^2$, where R is the Raman tensor, and $\hat{e}_i$ and $\hat{e}_s$ represent the polarization vectors of the incident and scattered light, respectively [19,20]. The Raman tensors for the A_g and B_g phonons for the given point symmetry group are represented as: $R(A_g) = \begin{pmatrix} a & 0 & d \\ 0 & b & 0 \\ d & 0 & c \end{pmatrix}$ and $R(B_g) = \begin{pmatrix} 0 & e & 0 \\ e & 0 & f \\ 0 & f & 0 \end{pmatrix}$.

Using circular polarizations $\sigma_R = [1 \quad -i \quad 0]/\sqrt{2}$ and $\sigma_L = [1 \quad i \quad 0]/\sqrt{2}$, the Raman intensity of the A_g mode is given as $I_{A_g}(\sigma_R\sigma_R) \sim |a+b|^2/4$ for the cocircular ($\sigma_R\sigma_R$) configuration, and $I_{A_g}(\sigma_R\sigma_L) \sim |a-b|^2/4$ for the cross-circular ($\sigma_R\sigma_L$) polarization configuration. Previous linearly polarized Raman studies on the MPX_3 family [21] have shown $a \cong b$, suggesting that the A_g modes are active only in the cocircular configuration. Conversely, the Raman intensity of the B_g mode is given by $I_{B_g}(\sigma_R\sigma_R) \sim 0$ for the cocircular configuration and $I_{B_g}(\sigma_R\sigma_L) \sim e^2$ for the cross-circular configuration, suggesting that the B_g mode is predominantly allowed in the cross-circular polarization channel.

Figure 1(a) shows the unpolarized Raman spectra of $NiPS_{3-x}Se_x$ collected at 3.5 K. The observed phonon excitations in the frequency range of $80 - 650\,\text{cm}^{-1}$ are labeled as B_g^k ($k = 1$–5) and A_g^i ($i = 1$–3), being in line with those for the parent $NiPS_3$ [2,9,22]. The low-frequency $B_g^1 \sim 134\ \text{cm}^{-1}$ and $B_g^2 \sim 180\ \text{cm}^{-1}$ modes are attributed to vibrations involving Ni^{2+} ions, while the phonon modes above $200\ \text{cm}^{-1}$ are mainly associated with vibrations of the $[P_2X_6(X = S, Se)]^{4-}$ cluster. At low temperatures, particularly below T_N, the B_g^2 mode splits into two distinct peaks with a separation energy of $\Delta\omega \approx 3\,\text{cm}^{-1}$ at 3.5 K for $x = 0.03$. This splitting is attributed to magnetic-order-induced symmetry breaking, which lifts the threefold rotational symmetry of the lattice [2]. As Se concentration increases from $x = 0.03$ to higher Se content, the split peaks overlap for $x > 0.03$, see Fig. 1(c). In contrast to linearly polarized Raman spectra [7], no splitting of B_g^2 is observed under circularly polarized Raman measurements. Rather, only a single peak appears in the cross-circular configuration, see Fig. 1(b). B_g^2 as well as other phonon modes including the A_g^i ($i = 1$–3) phonon excitations exhibit broadening with increasing Se substitution. For example, Figs. 1(d) and 1(e) display clear broadening for the A_g^1 and A_g^2 mode, respectively. In addition to the broadening, all phonon modes systematically soften as the Se content increases. Qualitatively, the reduction in vibrational frequencies can be understood by the substitution of lighter S atoms with heavier Se atoms, which increases the atomic mass and reduces the lattice stiffness.

Furthermore, a relatively broad peak, compared to the first-order phonon excitations in the $80 - 650\,\text{cm}^{-1}$ frequency range, appears in the cocircularly polarized configuration. This peak, labeled as R and centered at $\sim 446\,\text{cm}^{-1}$, is tentatively assigned to A_g symmetry. Additionally, in contrast to the parent $NiPS_3$, two additional peaks $P_1 \sim 354\,\text{cm}^{-1}$ and $P_2 \sim 524\,\text{cm}^{-1}$, gain spectral weight with increasing Se concentration and are observed in the cocircularly polarized configuration, see Figs. 1(a) and 1(b), indicating that their origin is associated with the vibrations of the $[P_2Se_6]^{4-}$ cluster in $NiPSe_3$. A group of phonons, labeled as S1–S6 in the frequency range of $685 - 900\,\text{cm}^{-1}$, see Fig. 1(a), have been identified as second-order phonon excitations in earlier Raman studies [23]. These S1–S6 phonon excitations are observed in the cocircular polarized configuration, reflecting that these exhibit A_g symmetry.

A broad continuum (marked by the blue shaded area), appears in the cross-circularly polarized configuration and is attributed to the two-magnon ($2M$) excitation [2,24], indicating the B_g/E_g characteristics of the $2M$ excitation, see Fig. 1(b). We note that in antiferromagnets, two magnons can be created with a total spin angular momentum change of $\Delta S = 0$, giving rise to a continuum of states involving all possible pairs of magnons with opposite momenta. Figures 2(a)–2(c) display the thermal evolution of these $2M$ excitations for $NiPS_{3-x}Se_x$ ($x = 0.03$, 0.06, and 0.9) in the frequency range of $5 - 900\,\text{cm}^{-1}$. With increasing temperature, the coherent $2M$ excitations, centered at finite energy, gradually weaken and soften. In the high-temperature paramagnetic state, the $2M$ signal evolves into a QES response, reflecting incoherent slow spin fluctuations. A close look reveals that this QES persists even within the magnetically ordered state, which is distinct from Rayleigh scattering.

Further, to highlight the low-energy features, we first obtain the Raman response $\chi''(\omega)$ from the raw Raman intensity $I(\omega)$ using the relation $I(\omega) \propto \chi''(\omega)\,[n(\omega) + 1] =$

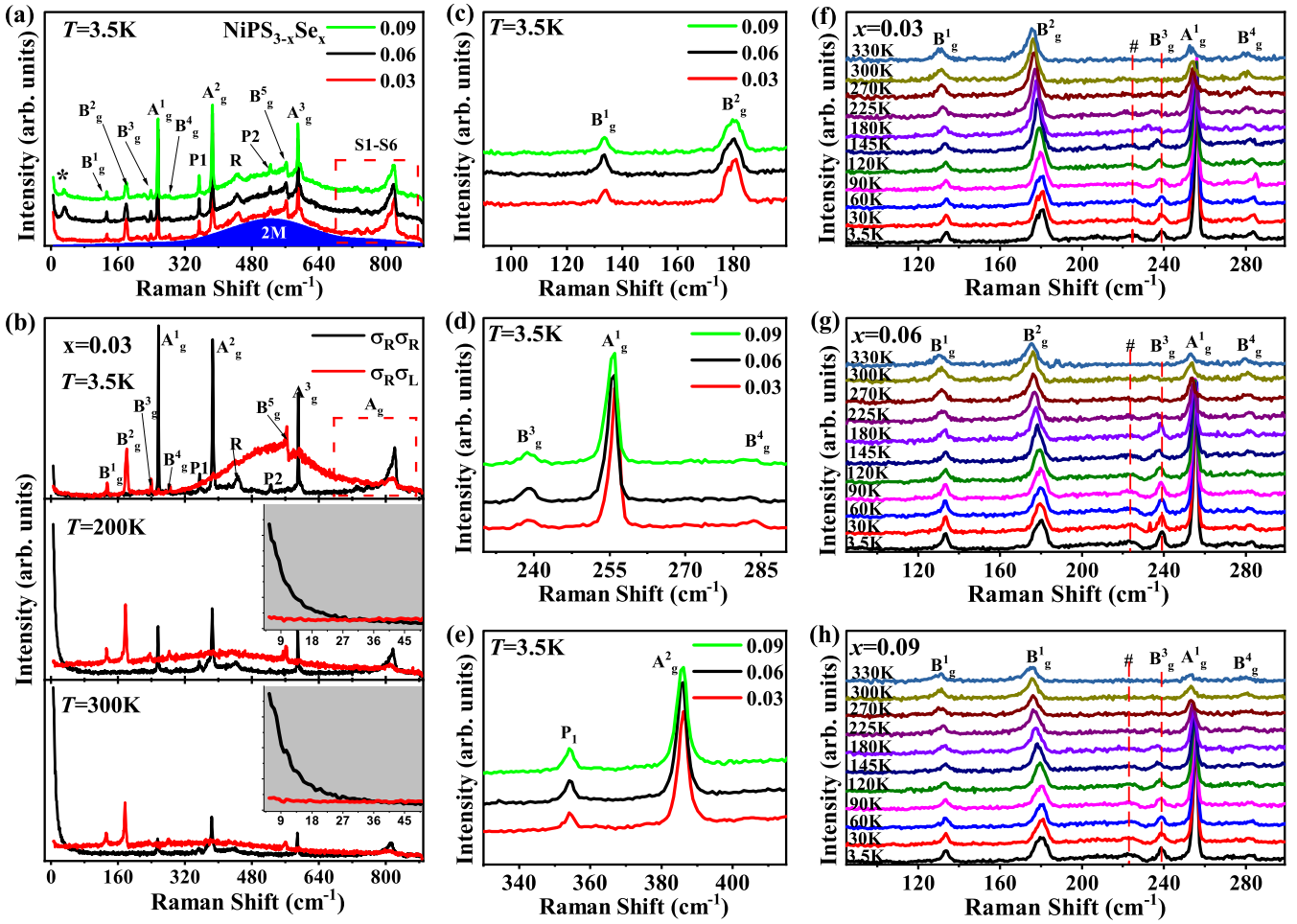

FIG. 1. (a) Unpolarized Raman spectrum of $NiPS_{3-x}Se_x$ ($x = 0.03$, 0.06, and 0.09) collected at 3.5 K in the frequency range of $5 - 900\,cm^{-1}$. The observed phonon excitations in a spectral range of $100 - 650\,cm^{-1}$ are labeled as B_g^{1-5}, A_g^{1-3}, R, and P1–P2. The phonon modes in the spectral range of $680 - 690\,cm^{-1}$ are labeled as S1–S6. The blue-shaded area corresponds to the two-magnon ($2M$) continuum. **(b)** Circularly polarized Raman spectrum for $x = 0.03$, collected at 3.5 K, 200 K, and 300 K in cocircularly ($\sigma_R\sigma_R$; black) and cross-circularly ($\sigma_R\sigma_L$; red) configurations. (c), (d), and (e) Raman spectrum of $NiPS_{3-x}Se_x$ in the frequency range of $8 - 200\,cm^{-1}$, $200 - 300\,cm^{-1}$, and $300 - 450\,cm^{-1}$, respectively. (f)–(h) Temperature evolution of the unpolarized Raman spectrum of $NiPS_{3-x}Se_x$ in the frequency range of $80 - 300\,cm^{-1}$.

$\chi''(\omega)\,[1 - e^{-\hbar\omega/k_BT}]$, and then plot the Raman conductivity ($\frac{\chi''(\omega)}{\omega}$) over the frequency range of $5 - 50\,cm^{-1}$ in Figs. 2(d)–2(f). It is evident that the QES response becomes systematically enhanced as the temperature is lowered from 300 K to 3.5 K for all compositions investigated. Additionally, we notice that a peak centered around $30\,cm^{-1}$ appears for $x \geqslant 0.06$ whose intensity increases with temperature but vanishes abruptly above 50 K. However, this peak is not consistently detected across all sample pieces, making its origin unclear. It is worth noting that the appearance of peaks below $60\,cm^{-1}$ in $NiPS_3$ has been previously discussed in terms of various scenarios, including spin gaps, breathing modes, and translational-symmetry-broken excitations [2,25–27].

B. Quasi-elastic scattering and magnetic energy fluctuations

Next, we elaborate on the dynamical magnetic properties and spin fluctuations by analyzing the QES. Generally, QES arises from either spin diffusion or fluctuations in magnetic energy densities. The first mechanism results in a Gaussian line shape and is forbidden in perfect one-dimensional materials, while the latter mechanism leads to a Lorentzian line shape [12] and is particularly relevant for magnetic materials with non-negligible spin-phonon coupling. We observe the QES in the low-frequency region (roughly below $40\,cm^{-1}$) of the Raman spectrum at higher temperatures, especially above T_N, where it is well described by a Lorentzian function implying that the fluctuations in magnetic energy density provide a dominant contribution. However, at lower temperatures within the magnetically ordered phase, the QES response deviates from the Lorentzian line shape and appears to transition into a composite profile exhibiting both Lorentzian and Gaussian characteristics, especially below 50 K. Circularly polarized Raman measurements, shown in Fig. 1(b), suggest that the QES response exhibits characteristics of A_g symmetry.

Figures 3(a)–3(c) show the color contour maps illustrating the evolution of QES spectral weight versus Raman shift across a temperature range of $T = 3.5$–330 K for $x = 0.03$, 0.06, and 0.09, respectively. We observe that the QES response gains spectral weight with increasing temperature and

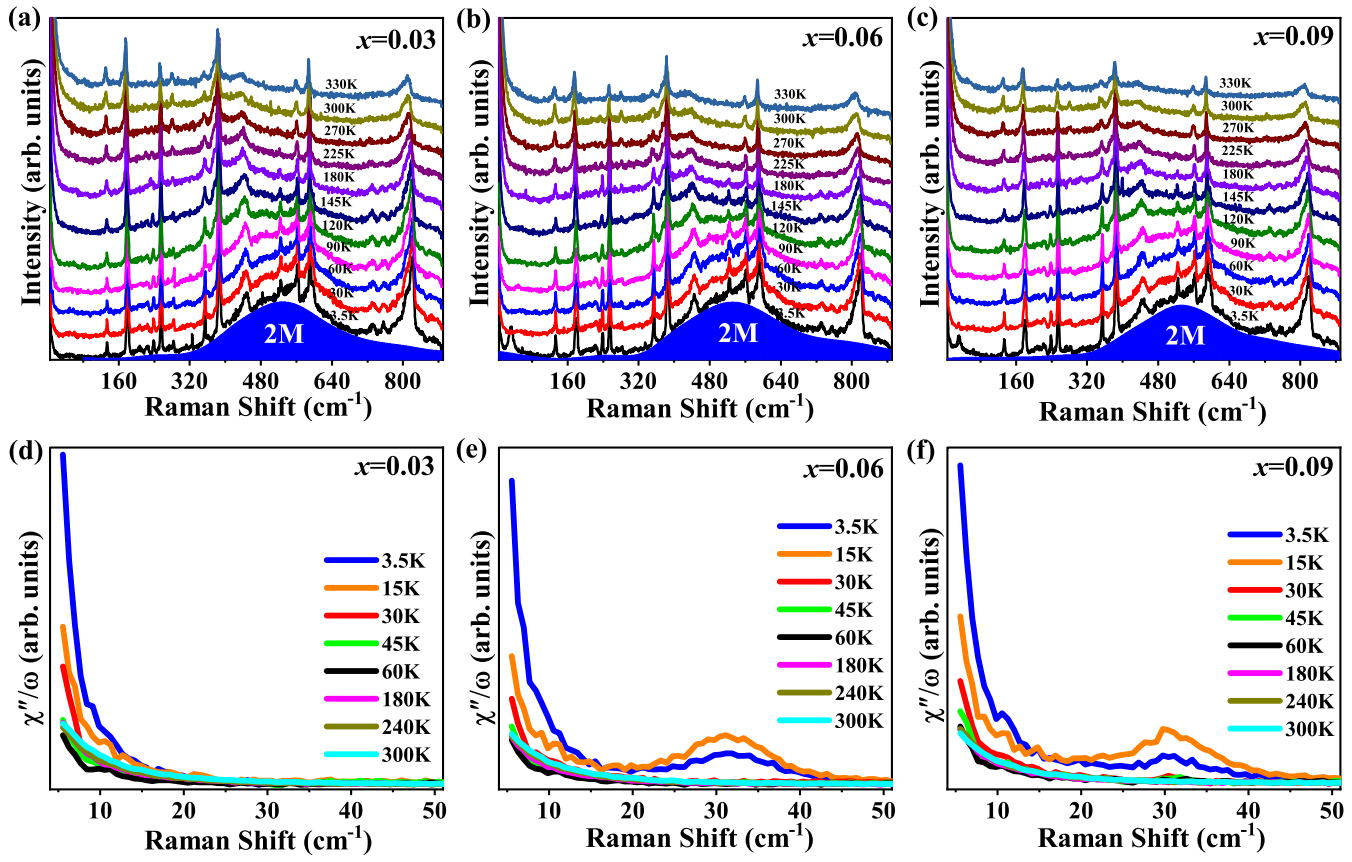

FIG. 2. Temperature evolution of the unpolarized Raman spectrum of $NiPS_{3-x}Se_x$ in the frequency range of $5-900\,cm^{-1}$ for (a) $x = 0.03$, (b) $x = 0.06$, and (c) $x = 0.09$. The blue-shaded area corresponds to the two-magnon ($2M$) continuum. (d)–(f) Raman conductivity of $NiPS_{3-x}Se_x$ (χ''/ω) at a few selected temperatures for $x = 0.03$, $x = 0.06$, and $x = 0.09$, respectvily.

becomes significant above T_N in the paramagnetic phase. As plotted in Fig. 4(a), the integrated spectral weight of the QES response shows a slight decrease from 3.5 to ~ 50 K, followed by a moderate increase between 50 K and ~ 120 K. Upon further heating into the paramagnetic regime, a sharp rise in spectral weight is observed. On the other hand, the Raman conductivity χ''/ω gains a significant spectral weight below 50 K, which is quite unexpected because χ''/ω is expected to be suppressed in the magnetically ordered phase in conventional magnetic systems. Furtheremore, χ''/ω shows a slight dependence in the temperature window from 50 K to T_N. Above T_N, the spectral weight of Raman conductivity increases with rising temperature. Nevertheless, the spectral weight of the Raman conductivity below 50 K is significantly larger than that at higher temperatures.

We note that in the magnetically ordered phase, conventional long-wavelength spin waves are expected. However, in addition to these well-defined magnons, Raman scattering at $Q \approx 0$ can also probe slow fluctuations of the ordered magnetic moments, particularly in low-dimensional antiferromagnets where frustration, anisotropy, or doping-induced disorder are present. Accordingly, the observed QES signal originates from overdamped, low-energy spin fluctuations that persist even in the ordered state. Such fluctuations may arise from competing exchange interactions or partial disruption of spin order induced by Se substitution.

Furthermore, we recall that the QES and the associated critical magnetic properties can be understood within the theoretical framework proposed by Reiter and Halley. According to their theory, the scattering intensity at a finite temperature for the two-spin scattering process can be expressed as [28,29]

$$I(\omega) = \int_{-\infty}^{\infty} e^{-i\omega t} dt \langle E(k,t)E^*(k,0)\rangle, \tag{1}$$

where $E(k,t)$ is the magnetic energy density. Considering the specific condition of the correlation function $\langle E(k,t)E^*(k,0)\rangle$, Eq. (1) can be simplified to [29]

$$I(\omega) \propto \frac{\omega}{1-e^{-\hbar\omega/k_BT}} \frac{C_m T D k^2}{\omega^2 + (Dk^2)^2}, \tag{2}$$

where C_m is the magnetic specific, D is the thermal diffusion constant $D = K/C_m$ related to the magnetic contribution to the thermal conductivity K. Further, Eq. (2) can be rewritten in terms of the Raman conductivity ($\frac{\chi''(\omega)}{\omega}$)

$$\frac{\chi''(\omega)}{\omega} \propto \frac{C_m T D k^2}{\omega^2 + (Dk^2)^2}. \tag{3}$$

We next deduce the dynamic Raman susceptibility (χ^{dyn}) from the Raman conductivity using the Kramers-Kronig relation: $\chi^{dyn}(q=0,T) = \frac{2}{\pi}\int_{-\infty}^{\infty} \frac{\chi''(\omega,T)}{\omega} d\omega$. To derive χ^{dyn},

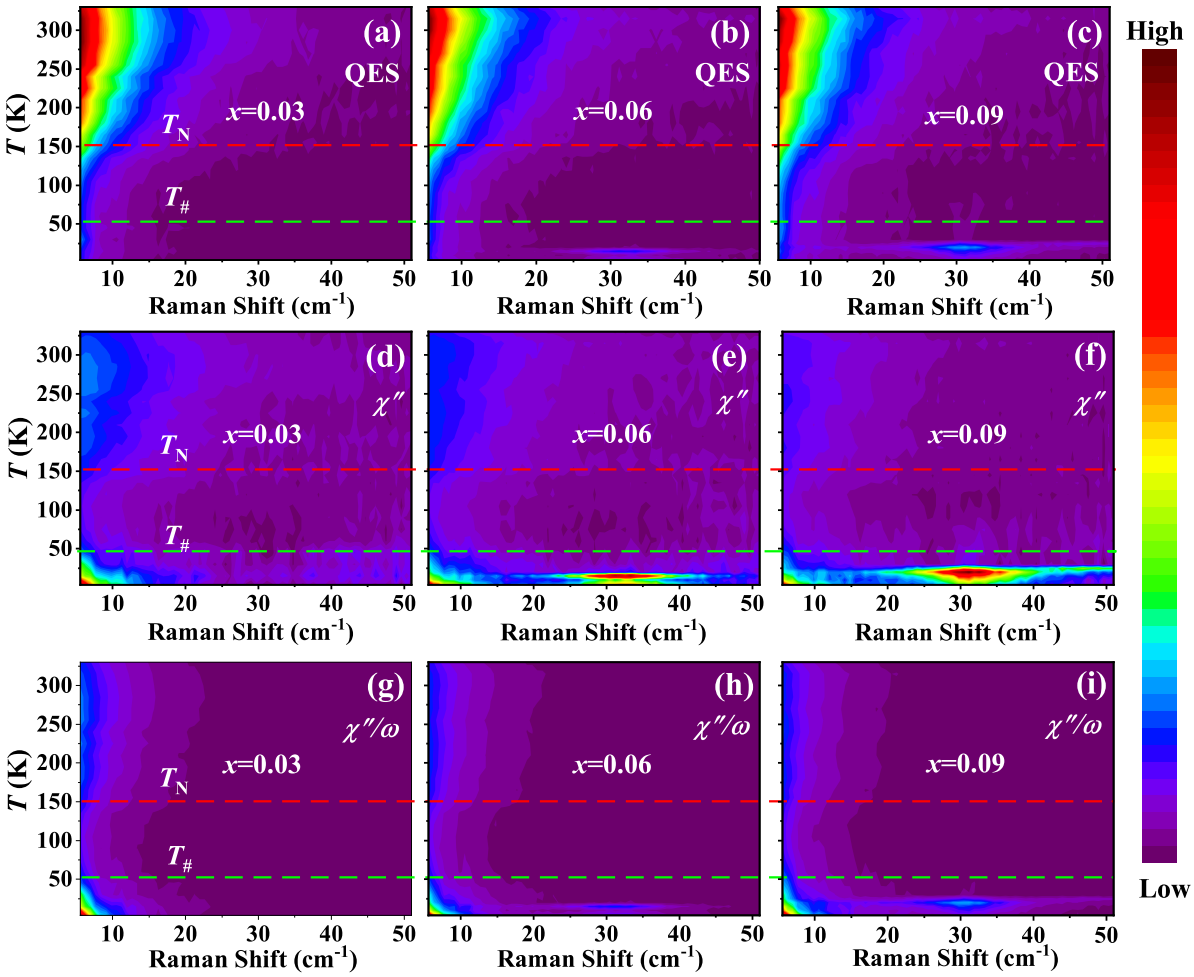

FIG. 3. Color contour maps of the QES spectral weight versus Raman shift and as a function of temperature for $NiPS_{3-x}Se_x$ series (a) $x = 0.03$, (b) $x = 0.06$, and (c) $x = 0.09$. (d)–(f) Color contour maps for the temperature dependence of the Raman response [$\chi'' \propto I(\omega)/1 + n(\omega)$] versus Raman shift. (g)–i) Color contour maps for the temperature dependence of Raman conductivity (χ''/ω) versus Raman shift. Red vertical dashed lines correspond to the Néel temperature (T_N). The green line represents the fluctuations of ordered magnetic moments phase transition temperature.

we adopted the upper cutoff frequency of ∼50 cm^{-1}, above which the Raman conductivity shows no noticeable change with further increase in frequency, while the lower cutoff frequency was taken as ∼5 cm^{-1}. Figure 4(b) shows the χ^{dyn} as a function of temperature and Se composition. For all samples, we observe a sharp decrease in χ^{dyn} from 3.5 K to 50 K, followed by a minimum around ∼90, ∼100 and ∼120 K for $x = 0.03$, 0.06, and 0.09, respectively. Upon further heating, χ^{dyn} increases through T_N and eventually shows the broad maximum-like behavior in the paramagnetic phase. Overall, the χ^{dyn} behavior resembles the static magnetic susceptibility data, as discussed in our work [7]. Unlike the static magnetic susceptibility, the low-temperature rise of χ^{dyn} in the magnetically ordered state arises from fluctuations of the ordered magnetic moments [30–33]. Before proceeding, we would like to comment that the QES exhibits a notable decrease at elevated temperatures. This behavior arises from two interrelated effects of Se substitution. First, Se substitution weakens the in-plane vs. out-of-plane spin interaction anisotropy due to altered Ni-S/Se-Ni superexchange pathways, promoting isotropic spin fluctuations. Second, chemical disorders from Se incorporation may dampen paramagnetic fluctuations through spin scattering at substitution sites.

Next, we deduce the magnetic specific heat, above T_N, from the Raman conductivity using Eq. (3), and the results are summarized in Fig. 4(c). For all samples, we observe a decrease in the magnetic specific heat with a rise in temperature. Figure 4(d) shows the temperature dependence of the spin correlation length (ξ) above T_N obtained from the Raman conductivity by taking the inverse of the FWHM of the Lorentzian profile. We found that ξ follows a temperature dependence trend similar to that of the magnetic-specific heat.

C. Temperature-dependent Raman scattering intensity

Now, we turn to the temperature dependence of phonon mode intensities. In magnetic materials, intensity variations offer valuable insights into the role of spin degrees of freedom in the Raman scattering process. Suzuki and Kamimura (SK) proposed a theory to describe the phonon intensity in magnetic materials. According to the SK theory, the temperature-

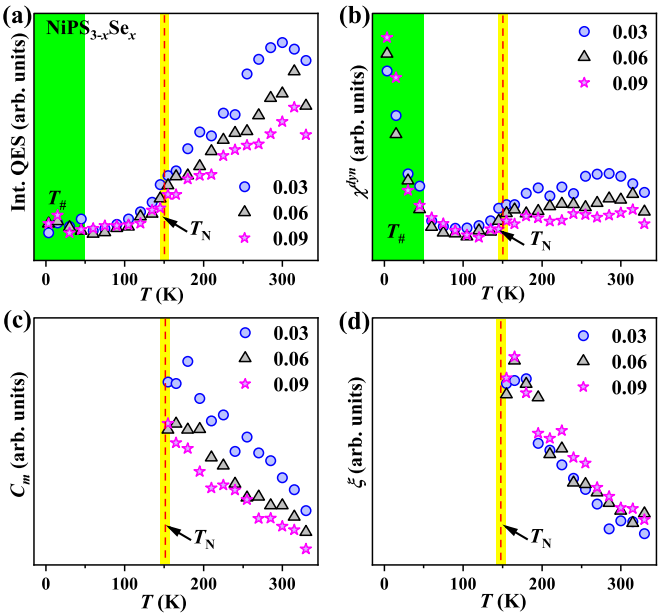

FIG. 4. (a) Temperature dependence of the integrated QES spectral weight. (b) Temperature dependence of the dynamic Raman susceptibility, obtained using the Kramers-Kronig relation $\chi^{\rm dyn}(q=0,T)=\frac{2}{\pi}\int_{-\infty}^{\infty}\frac{\chi''(\omega,T)}{\omega}d\omega$. The peak centered around $\sim 30\,{\rm cm}^{-1}$ was exluded while integrating out the QES and dynamic Raman susceptibility. The red vertical dashed line corresponds to the $T_{\rm N}$. The green shaded area marks the temperature regime where the fluctuations of the ordered magnetic moment are enhanced. (c) and (d) Magnetic specific heat and spin-correlation length as a function of temperature extracted above $T_{\rm N}$, respectively.

dependent phonon intensity is given as [34]

$$I(T)=(n+1)\left[\left|R+M\frac{\langle\vec{S_i}\cdot\vec{S_j}\rangle}{S^2}\right|^2+|K|^2\langle S_z^2\rangle\right]. \quad (4)$$

Here, the coefficient M quantifies the spin-dependent contribution to the Raman scattering intensity through spin-spin correlations $\langle\vec{S_i}\cdot\vec{S_j}\rangle$ between magnetic ions at the ith and jth sites, while the coefficient R accounts for the spin-independent contribution. The term $|K|^2\langle S_z^2\rangle$ is related to single-ion anisotropies and is usually neglected, as K is typically one or two orders of magnitude smaller than R and M. Consequently, the SK formula can be simplified to

$$I(T)=\left|R+M\frac{\langle\vec{S_i}\cdot\vec{S_j}\rangle}{S^2}\right|^2. \quad (5)$$

Figures 5(a)–5(c) present the color contour maps of the Raman intensity versus Raman shift in the $80-200\,{\rm cm}^{-1}$ range (left panel) and in the $200-300\,{\rm cm}^{-1}$ range (right panel) across a temperature window of 3.5–330 K for the $x=0.03, 0.06,$ and 0.09 samples. The integrated intensities of the B_g^1, B_g^2, and A_g^1 phonons are plotted in Figs. 5(d)–5(f). We observe that the B_g^1 mode becomes more intense at higher temperatures, particularly above $T_{\rm N}$, while the B_g^2 mode reaches its maximum intensity around $T_{\rm N}$, and then gradually weakens as the temperature rises above $T_{\rm N}$. This intensity behavior is distinct from that observed in other members of the MPX_3 family, where a significant enhancement in phonon intensity occurs below $T_{\rm N}$ [10,35–37]. However, the A_g^1 mode and other phonon excitations above $200\,{\rm cm}^{-1}$, except for the background peak around $\sim 446\,{\rm cm}^{-1}$, gradually weaken with increasing temperature from our lowest to highest recorded temperature, see Figs. 1, 2, and 5.

It is worth noting that the SK theory predicts three types of phonon intensity variations with temperature in ferromagnetic and antiferromagnetic materials, depending on the relative magnitudes of R/M. In antiferromagnetic systems, if the ratio R/M lies between 0 and 1, the phonon intensity decreases with temperature below $T_{\rm N}$, while upon further heating above $T_{\rm N}$, the intensity increases. Our experimental intensity data for B_g^1 are largely consistent with the aforementioned prediction. However, on the other hand, the B_g^2 mode becomes intense around $T_{\rm N}$, possibly due to the overlap of its split components. Furthermore, for $R/M<0$, the phonon intensity is expected to decrease with increasing temperature, which aligns with our experimental data for A_g^1 and other phonon excitations above $200\,{\rm cm}^{-1}$.

D. Magnetic ordering effects and spin-phonon coupling

Next, we inspect the temperature dependence of the phonon parameters. Figure 6 and Fig. 7 show the temperature-dependent frequencies and linewidths of the B_g^1, B_g^2, P1, A_g^1, and A_g^2 phonon excitations in the $NiPS_{3-x}Se_x$ series. For all samples, we observe that phonon excitations above $200\,{\rm cm}^{-1}$ exhibit softening and broadening with increasing temperature, which can be understood within the framework of the three-phonon anharmonicity model [38], which accounts for the decay of an optical phonon into two lower-energy phonons of opposite momentum. In this model, the temperature dependence of the phonon frequency $\omega(T)$ and linewidth $\Gamma(T)$ is described by: $\omega(T)=\omega_0+A\,(1+\frac{2}{e^x-1})$ and $\Gamma(T)=\Gamma_0+B\,(1+\frac{2}{e^x-1})$, where $x=\hbar\omega_0/2k_BT$ and ω_0 (Γ_0) is the frequency (linewidth) of the phonon at 0 K. The coefficients A and B are fitting parameters characterizing the strength of the anharmonic phonon-phonon interactions. The solid red lines in Fig. 7 represent the fitted curves based on this model, which shows a good agreement with the experimental data. This consistency suggests that the anharmonicity effect provides an adequate explanation for the observed temperature-induced softening and broadening of the high-frequency phonon modes. However, in contrast to the phonon excitations above $200\,{\rm cm}^{-1}$, the temperature-dependent frequencies of the lower-energy B_g^1 and B_g^2 modes deviate from the conventional anharmonicity-driven temperature dependence below $T_{\rm N}$ [see Fig. 6(a) and 6(c)]. This deviation is further accompanied by a linewidth maximum around 140 K for the B_g^1 mode and 100 K for the B_g^2 mode [see Fig. 6(b) and 6(d)], suggesting the involvement of additional mechanisms beyond simple three-phonon anharmonicity. It is worth recalling that spin-phonon coupling plays an important role in renormalizing the phonon self-energy parameters in magnetically ordered systems.

Within the spin-phonon coupling mechanism, the temperature dependence of the phonon frequency is written as

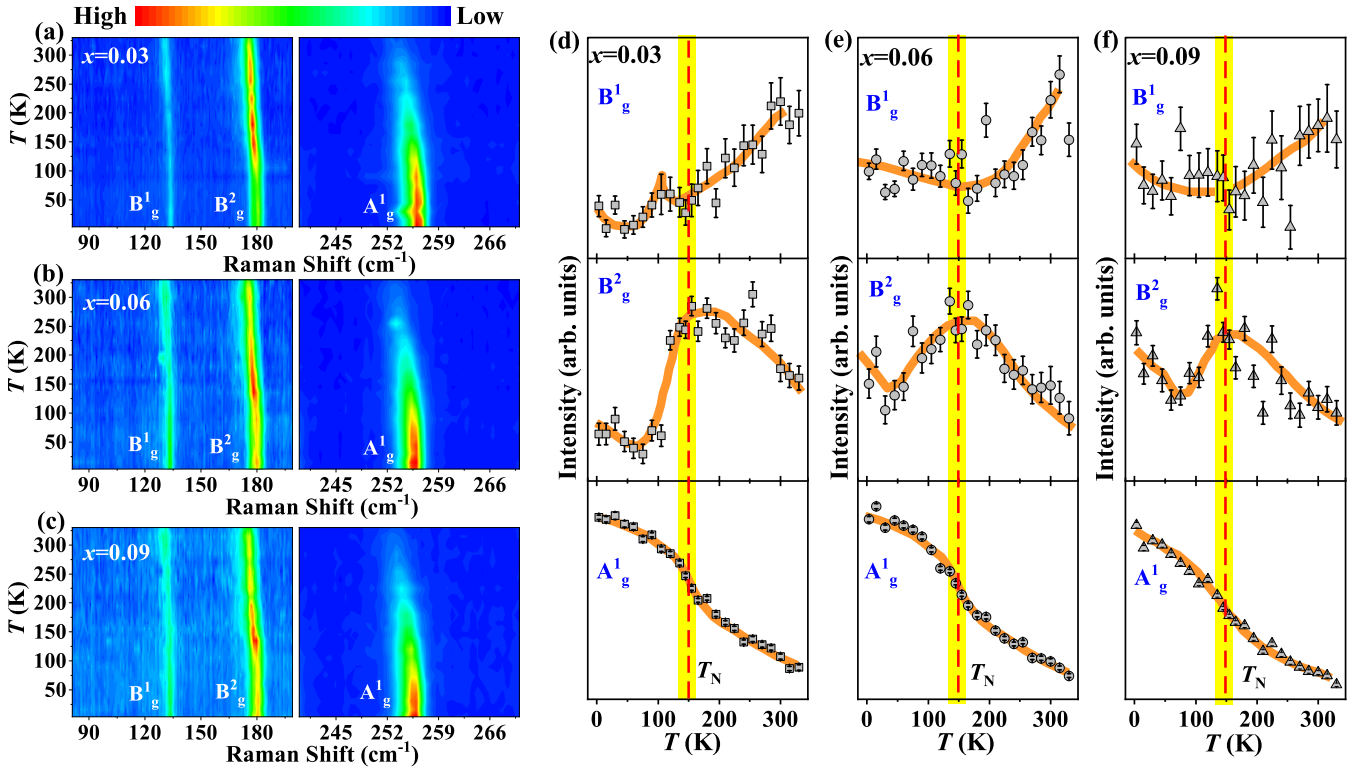

FIG. 5. 2D color contour maps of intensity as a function of temperature and frequency for (a) $x = 0.03$, (b) 0.06, and (c) 0.09 of the series, respectively. The left panel corresponds to the B_g^1 and B_g^2 modes, while the right panel corresponds to the A_g^1 mode. Temperature-dependent integrated intensity of the B_g^1, B_g^2, and A_g^1 modes for (d) $x = 0.03$, (e) 0.06, and (f) 0.09, respectively. Semitransparent broad lines are a guide to the eye. Red vertical dashed lines correspond to the T_N.

[39,40]$\Delta\omega_{\text{sp-ph}} = \omega_{\text{sp-ph}}(T) - \omega_0 = \lambda\langle \vec{S_i} \cdot \vec{S_j} \rangle$, where ω_0 is the bare phonon frequency in the absence of spin-phonon coupling, and λ is the spin-phonon coupling constant, which quantifies the interaction strength between phonons and spins in the materials. In this framework, the bare phonon frequency is renormalized by the spin-spin correlations $\langle \vec{S_i} \cdot \vec{S_j} \rangle$ through spin-phonon coupling λ. Within the mean-field approximation, the spin-spin correlations $\langle \vec{S_i} \cdot \vec{S_j} \rangle$ can be approximated as $\langle \vec{S_i} \cdot \vec{S_j} \rangle = -S^2\phi(T)$, where S is the spin of the magnetic ions and $\phi(T)$ is the magnetic order parameter. Near the transition temperature, the order parameter follows a power-law behavior $\phi(T) = 1 - (\frac{T}{T_N})^{\gamma}$, where γ is the critical exponent associated with the magnetic phase transition.

For $x = 0.03$, we observed the anomalous hardening in the B_g^2 mode below T_N, see Fig. 6(c), which likely originates from the spin-phonon coupling [41,42]. With increasing Se concentration, i.e. $x > 0.03$, a renormalization in slope is observed, suggesting that chalcogen substitution modulates the spin-phonon coupling strength. Similar to B_g^2, anomalous hardening or softening is also observed in the B_g^1 mode below T_N, see Fig. 6(a). These results are consistent with the temperature-dependent QES components, Raman conductivity, and the spectral weight of the dynamic Raman susceptibility. All of these quantities weaken, especially at higher temperatures with an increase in Se concentration. We note that spin-phonon coupling and QES are intrinsically interconnected: stronger spin-phonon coupling leads to more pronounced QES, as lattice distortions induced by spin-phonon interactions can, in turn, drive magnetic spin fluctuations, or vice versa.

III. CONCLUSIONS

To summarize, we have investigated low-energy magnetic excitations and lattice dynamics in anion-substituted van der Waals antiferromagnets $NiPS_{3-x}Se_x$ using temperature- and polarization-dependent Raman spectroscopy. A clear quasi-elastic scattering signal is detected in the cocircular polarization channel, whose Lorentzian line shape above the Néel temperature is attributed to spin energy density fluctuations in the paramagnetic phase. Below T_N (~ 50 K), the quasi-elastic spectral weight intensifies and deviates from the Lorentzian profile, indicating enhanced fluctuations of the magnetic moment even in the ordered phase. Concurrently, phonon modes involving Ni^{2+} exhibit anomalous shifts below T_N, providing strong evidence of spin-phonon coupling. The systematic evolution of the quasi-elastic response and phonon anomalies with increasing Se concentration ($x = 0.03$, 0.06, 0.09) highlight the importance of dynamic spin correlations in the ordered phase and demonstrate the chemically tuned spin fluctuations.

ACKNOWLEDGMENTS

This work was supported by the National Research Foundation (NRF) of Korea (Grants No. 2020R1A5A1016518,

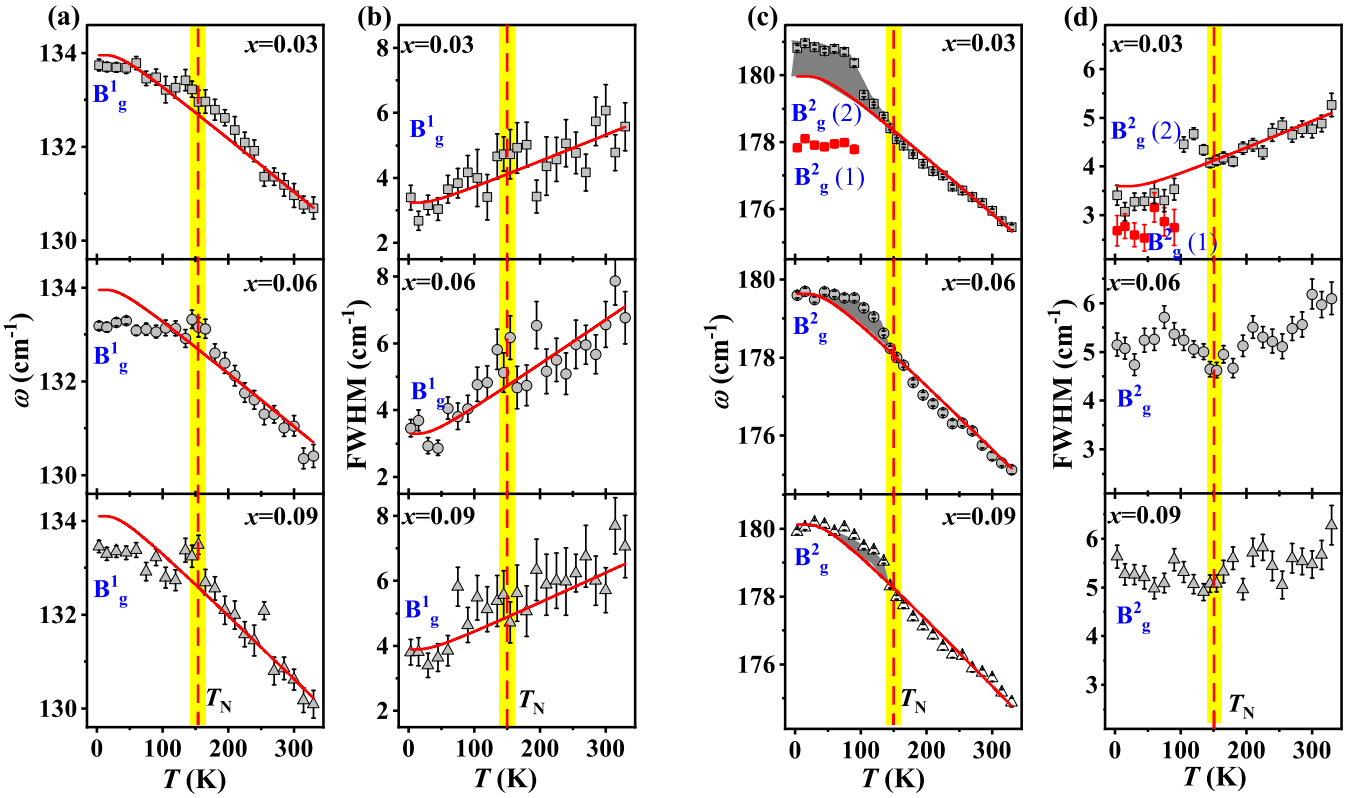

FIG. 6. (a), (b) Temperature-dependent frequency and linewidth of the B_g^1 for $x = 0.03$ (top), 0.06 (middle), and 0.09 (bottom) panel. (c), (d) Temperature-dependent frequency and linewidth of the B_g^2 for $x = 0.03$ (top), 0.06 (middle), and 0.09 (bottom) panel. Solid red lines are the fitted curves as described in the text. Red vertical dashed lines correspond to the T_N. Gray shaded area in (c) below T_N indicate the spin-phonon coupling regime.

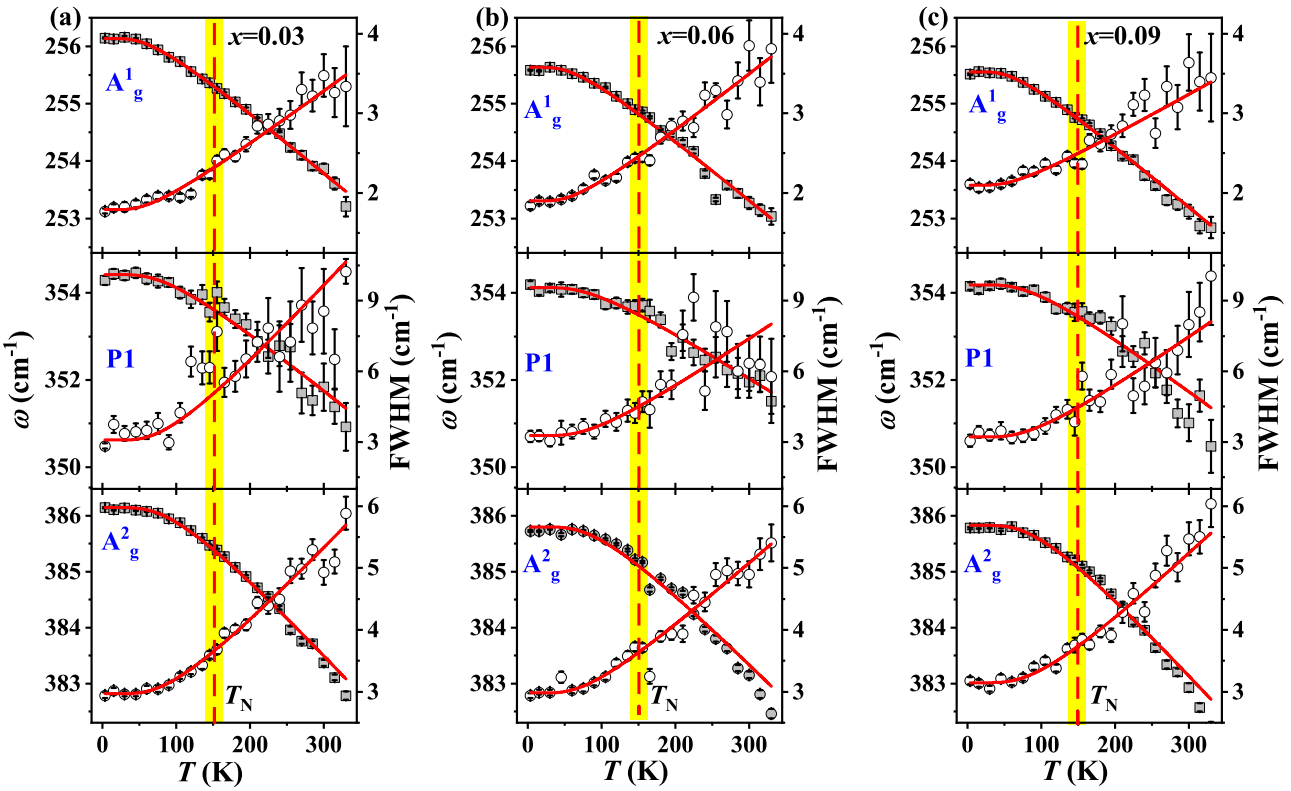

FIG. 7. (a)–(c) Temperature-dependent frequency (square) and FWHM (circle) of the A_g^1, P1, and A_g^2 phonon excitations for $NiPS_{3-x}Se_x$ series. Solid red lines are the fitted curve as described in the main text. The red vertical dashed line corresponds to the T_N.

No. RS-2020-NR049536, and No. RS-2023–00209121). R.S. acknowledges the financial support provided by the Ministry of Science and Technology in Taiwan under Project No. NSTC (113–2124-M-001–045-MY3 and 113–2124-M-001–003), Financial support from the Center of Atomic Initiative for New Materials (AI-Mat), National Taiwan University, (Project No. 113L900801) and Academia Sinica for the budget of AS-iMATE-113–12. R.K.U. would like to acknowledge the IITR for the Faculty Initiation Grant (FIG-101068).

DATA AVAILABILITY

The data that support the findings of this article are not publicly available. The data are available from the authors upon reasonable request.

[1] P. A. Joy and S. Vasudevan, Magnetism in the layered transition-metal thiophosphates MPS_3 (M = Mn, Fe, and Ni), Phys. Rev. B **46**, 5425 (1992).

[2] K. Kim, S. Y. Lim, J. U. Lee, S. Lee, T. Y. Kim, K. Park, G. S. Jeon, C. H. Park, J. G. Park, and H. Cheong, Suppression of magnetic ordering in XXZ-type antiferromagnetic monolayer $NiPS_3$, Nature Commun. **10**, 345 (2019).

[3] R. Basnet, K. M. Kotur, M. Rybak, C. Stephenson, S. Bishop, C. Autieri, M. Birowska, and J. Hu, Controlling magnetic exchange and anisotropy by nonmagnetic ligand substitution in layered MPX_3 (M = Ni, Mn; X = S, Se), Phys. Rev. Res. **4**, 023256 (2022).

[4] D. Lançon, H. C. Walker, E. Ressouche, B. Ouladdiaf, K. C. Rule, G. J. McIntyre, T. J. Hicks, H. M. Rønnow, and A. R. Wildes, Magnetic structure and magnon dynamics of the quasi-two-dimensional antiferromagnet $FePS_3$, Phys. Rev. B **94**, 214407 (2016).

[5] J. K. Kim, W. Na, J. Kim, P. Park, K. Zhang, I. Hwang, Y. W. Son, J. H. Kim, H. Cheong, and J. G. Park, Rapid Suppression of quantum many-body magnetic exciton in doped van der Waals antiferromagnet (Ni, Cd)PS_3, Nano Lett. **23**, 10189 (2023).

[6] J. H. Lee, S. Lee, Y. Choi, L. Gries, R. Klingeler, K. Raju, R. K. Ulaganathan, R. Sankar, M. J. Seong, and K. Y. Choi, Optical probe of magnetic ordering structure and spin-entangled excitons in Mn-substituted $NiPS_3$, Adv. Funct. Mater. **34**, 2405153 (2024).

[7] D. Kumar, J. Khatua, N. T. Hoang, Y. Sim, R. K. Ulaganathan, R. Kalaivanan, R. Sankar, M.-J. Seong, and K.-Y. Choi, Manipulation of anisotropic Zhang-Rice exciton in van der Waals antiferromagnets $NiPS_{3-x}Se_x$ by anion substitution, npj 2D Mater. Appl. **9**, 87 (2025).

[8] R. Oliva, E. Ritov, F. Horani, I. Etxebarria, A. K. Budniak, Y. Amouyal, E. Lifshitz, and M. Guennou, Lattice dynamics and in-plane antiferromagnetism in $Mn_xZn_{1-x}PS_3$ across the entire composition range, Phys. Rev. B **107**, 104415 (2023).

[9] N. Khan, D. Kumar, V. Kumar, Y. Shemerliuk, S. Selter, B. Büchner, K. Pal, S. Aswartham, and P. Kumar, The interplay of topology and antiferromagnetic order in two-dimensional van der Waals crystals of The interplay of topology and antiferromagnetic order in two-dimensional van der Waals crystals of $(Ni_xFe_{1-x})_2P_2S_6$, 2D Mater. **11**, 035018 (2024).

[10] D. Kumar, N. T. Hoang, Y. Sim, Y. Choi, K. Raju, R. K. Ulaganathan, R. Sankar, M. J. Seong, and K. Y. Choi, Interplay between magnetic and lattice excitations and emergent multiple phase transitions in $MnPSe_{3-x}S_x$, Phys. Rev. B **110**, 064414 (2024).

[11] H. Han, H. Lin, W. Gan, Y. Liu, R. Xiao, L. Zhang, Y. Li, C. Zhang, and H. Li, Emergent mixed antiferromagnetic state in $MnPS_{3(1-x)}Se_{3x}$, Appl. Phys. Lett. **122**, 033101 (2023).

[12] P. Lemmens, G. Güntherodt, and C. Gros, Magnetic light scattering in low-dimensional quantum spin systems, Phys. Rep. **375**, 1 (2003).

[13] I. Yamada and H. Onda, Light scattering from magnetic-energy fluctuations in the one-dimensional Heisenberg antiferromagnet $KCuF_3$, Phys. Rev. B **49**, 1048 (1994).

[14] T. Sekine, M. Jouanne, C. Julien, and M. Balkanski, Light-scattering study of dynamical behavior of antiferromagnetic spins in the layered magnetic semiconductor $FePS_3$, Phys. Rev. B **42**, 8382 (1990).

[15] R. Rao, R. Selhorst, R. Siebenaller, A. N. Giordano, B. S. Conner, E. Rowe, and M. A. Susner, Mode-selective spin–phonon coupling in van der Waals antiferromagnets, Adv. Phys. Res. **3**, 2300153 (2024).

[16] N. Khan, D. Kumar, S. Semwal, Y. Shemerliuk, B. Büchner, K. Pal, S. Aswartham, and P. Kumar, Short and long-range magnetic ordering and emergent topological transition in $(Mn_{1-x}Ni_x)_2P_2S_6$, Sci. Rep. **15**, 4438 (2025).

[17] S. Yan, W. Wang, C. Wang, L. Chen, X. Ai, Q. Xie, and G. Cheng, Anharmonic phonon scattering study in $MnPS_3$ crystal by Raman spectroscopy, Appl. Phys. Lett. **121**, 032203 (2022).

[18] A. Hashemi, H. P. Komsa, M. Puska, and A. V. Krasheninnikov, Vibrational properties of metal phosphorus trichalcogenides from first-principles calculations, J. Phys. Chem. C **121**, 27207 (2017).

[19] M. Cardona and G. Guntherodt, *Light Scattering in Solids II - Basic Concepts and Instrumentation* (Springer, Berlin, 1982), Vol. 50.

[20] R. Loudon, The Raman effect in crystals, Adv. Phys. **50**, 813 (2001).

[21] K. Kim, S. Y. Lim, J. Kim, J. U. Lee, S. Lee, P. Kim, K. Park, S. Son, C. H. Park, J. G. Park, and H. Cheong, Antiferromagnetic ordering in van der Waals 2D magnetic material $MnPS_3$ probed by Raman spectroscopy, 2D Mater. **6**, 041001 (2019).

[22] S. Lee, J. Park, Y. Choi, K. Raju, W. Chen, R. Sankar, and K. -Y. Choi, Chemical tuning of magnetic anisotropy and correlations in $Ni_{1-x}Fe_xPS_3$, Phys. Rev. B **104**, 174412 (2021).

[23] C. Kuo, T., M. Neumann, K. Balamurugan, H. J. Park, S. Kang, H. W. Shiu, J. H. Kang, B. H. Hong, M. Han, T. W. Noh, and J. G. Park, Exfoliation and raman spectroscopic fingerprint of few-layer $NiPS_3$ van der Waals crystals, Sci. Rep. **6**, 20904 (2016).

[24] S. Rosenblum, A. H. Francis, and R. Merlin, Two-magnon light scattering in the layered antiferromagnet $NiPS_3$ Spin-1/2-like anomalies in a spin-1 system, Phys. Rev. B **49**, 4352 (1994).

[25] D. Jana, P. Kapuscinski, I. Mohelsky, D. Vaclavkova, I. Breslavetz, M. Orlita, C. Faugeras, and M. Potemski, Magnon gap excitations and spin-entangled optical transition in the van der Waals antiferromagnet $NiPS_3$, Phys. Rev. B **108**, 115149 (2023).

[26] Z. Sun, G. Ye, C. Zhou, M. Huang, N. Huang, X. Xu, Q. Li, G. Zheng, Z. Ye, C. Nnokwe, L. Li, H. Deng, L. Yang, D. Mandrus, Z. Y. Meng, K. Sun, C. R. Du, R. He, and L. Zhao, Dimensionality crossover to a two-dimensional vestigial nematic state from a three-dimensional antiferromagnet in a honeycomb van der Waals magnet, Nature Phys. **20**, 1764 (2024).

[27] W. Na, P. Park, S. Oh, J. Kim, A. Scheie, D. A. Tennant, H. C. Lee, J. G. Park, and H. Cheong, Direct observation and analysis of low-energy magnons with raman spectroscopy in atomically thin $NiPS_3$, ACS. Nano **18**, 20482 (2024).

[28] G. F. Reiter, Light scattering from energy fluctuations in magnetic insulators, Phys. Rev. B **13**, 169 (1976).

[29] J. W. Halley, Light scattering as a probe of dynamical critical properties of antiferromagnets, Phy. Rev. Lett. **41**, 1605 (1978).

[30] Y. Choi, S. Lee, J. H. Lee, S. Lee, M. J. Seong, and K. Y. Choi, Bosonic spinons in anisotropic triangular antiferromagnets, Nature Commun. **12**, 6453 (2021).

[31] A. Glamazda, P. Lemmens, S. -H. Do, Y. S. Choi, and K. -Y. Choi, Raman spectroscopic signature of fractionalized excitations in the harmonic-honeycomb iridates β- and γ-Li_2IrO_3, Nature Commun. **7**, 12286 (2016).

[32] V. Kumar, D. Kumar, B. Singh, Y. Shemerliuk, M. Behnami, B. Büchner, S. Aswartham, and P. Kumar, Fluctuating fractionalized spins in quasi-two-dimensional magnetic $V_{0.85}PS_3$, Phys. Rev. B **107**, 094417 (2023).

[33] P. Mellado, and M. Sturla, Quantum fluctuations in the van der Waals material $NiPS_3$, Phys. Rev. B **110**, 134438 (2024).

[34] N. Suzuki, and H. Kamimura, Theory of spin-dependent phonon raman scattering in magnetic crystals, J. Phys. Soc. Jpn. **35**, 985 (1973).

[35] M. Scagliotti, M. Jouanne, M. Balkanski, G. Ouvrard, and G. Benedek, Raman scattering in antiferromagnetic $FePS_3$, and $FePSe_3$ crystals, Phys. Rev. B **35**, 7097 (1987).

[36] P. Liu, Z. Xu, H. Huang, J. Li, C. Feng, M. Huang, M. Zhu, Z. Wang, Z. Zhang, D. Hou, Y. Lu, and B. Xiang, Exploring the magnetic ordering in atomically thin antiferromagnetic $MnPSe_3$ by Raman spectroscopy, J. Alloys Compd. **828**, 154432 (2020).

[37] J. Qiu, W. J. Huang, Y. J. Lee, S. Kim, X. B. Chen, and I. S. Yang, Raman study of the spin–lattice excitations of the layered antiferromagnets $MPSe_3$ (M = Fe, Mn), Results Phys. **56**, 07256 (2024).

[38] P. G. Klemens, Anharmonic decay of optical phonon in diamond, Phys. Rev. B **11**, 3206 (1975).

[39] E. Granado, A. García, J. A. Sanjurjo, C. Rettori, I. Torriani, F. Prado, R. D. Sánchez, A. Caneiro, and S. B. Oseroff, Magnetic ordering effects in the Raman spectra of $La_{1-x}Mn_{1-x}O_3$, Phys. Rev. B **60**, 11879 (1999).

[40] M. N. Iliev, M. V. Abrashev, A. P. Litvinchuk, V. G. Hadjiev, H. Guo, and A. Gupta, Raman spectroscopy of ordered double perovskite La_2CoMnO_6 thin films, Phys. Rev. B **75**, 104118 (2007).

[41] Y. Tian, M. J. Gray, H. Ji, R. J. Cava, and K. S. Burch, Magneto-elastic coupling in a potential ferromagnetic 2D atomic crystal, 2D Mater. **3**, 025035 (2016).

[42] T. Yin, K. A. Ulman, S. Liu, A. Granados del Águila, Y. Huang, L. Zhang, M. Serra, D. Sedmidubsky, Z. Sofer, S. Y. Quek, and Q. Xiong, Chiral phonons and giant magneto-optical effect in $CrBr_3$, 2D Magnet Adv. Mater. **33**, 2101618 (2021).